Int. J. Electrochem. Sci., 15 **(2020)** 9874 – 9887, doi: 10.20964/2020.10.62

International Journal of
ELECTROCHEMICAL
SCIENCE
www.electrochemsci.org

Influence of Zinc and Aluminum Simultaneous Injection on Corrosion Behavior and Semiconducting Properties of Oxide Film on 304L

*Shenghan Zhang**, *Chenhao Sun, Yu Tan*

Hebei Key Lab of Power Plant Flue Gas Multi-Pollutants Control, Department of Environment Science and Engineering, North China Electric Power University, Baoding, 071003, PR China; Environmental Systems Optimization, College of Environmental Science and Engineering, North China Electric Power University, Beijing, 102206, PR China
*E-mail: shenghan_zhang@126.com

Received: 15 June 2020 / *Accepted:* 2 August 2020 / *Published:* 31 August 2020

Zinc and aluminum simultaneous injection technology aim to reduce the cost and potential radioactivity of traditional zinc injection technology by replacing a portion of the zinc used with aluminum. Oxide films on 304L SS were formed in a high-temperature water environment under simultaneous injection of zinc and aluminum, and their corrosion behavior and semiconducting properties were studied by potentiodynamic scanning, EIS, Mott-Schottky curve, SEM, XPS and GI-XRD analysis. The results showed that the oxide film formed by simultaneous injection of zinc and aluminum had a lower corrosion current and higher impedance; additionally, it had a more compact appearance and changes in its semiconducting properties. The corrosion resistance and stability of the oxide film were enhanced through injection of zinc and aluminum. Both zinc and aluminum were involved in the formation reactions of the oxide film and formed spinel phases of $ZnAl_2O_4$ and $ZnFe_2O_4$. In addition, a point defect model (PDM) was employed to microscopically describe the formation process of $ZnAl_2O_4$ in the oxide film and the change of semiconducting properties.

Keywords: Zinc and Aluminum Simultaneous Injection; 304L SS; Corrosion Behavior; Point Defect Model.

1. INTRODUCTION

Stainless steel (SS) is widely used in nuclear power plants[1, 2]. Oxide films will be formed on the surface of stainless steel in high temperature water of light water reactor (LWR) primary circuits[3, 4]. The stability of the oxide films is closely related to their corrosion resistance and the release of corrosion products[5, 6]. Therefore, the formation of a dense and stable oxide film on the metal substrate is essential for the improvement of metal corrosion resistance.

Zinc injection technology has been widely adopted to reduce the dose rates and to retard the corrosion of materials of pressurized water reactor (PWR) primary circuits[7]. It is generally considered that in PWR primary coolants with zinc injection, the oxide films formed on stainless steels and nickel-based alloys comprised some new stable phases of $ZnFe_2O_4$ and $ZnCr_2O_4$ which resulted in an improvement in the corrosion resistance of the alloys[8-10]. And the zinc can replace radionuclides, such as ^{60}Co and ^{58}Co, in the oxide films, which reduce the primary circuit dose rates[11, 12].

Since ^{64}Zn in natural zinc is easily activated to ^{65}Zn, expensive depleted zinc has to be used in zinc injection. While aluminum ion is inexpensive, not activated in LWR primary circuits and has obvious corrosion inhibition effects on steel in water[13]. In previous researches, addition of aluminum alone could slightly reduce the corrosion rate of 304L and 316L SS, but the effect was not obvious. Existence of Al^{3+} impeded the transport of the metal ion in the micropore and inhibited deposition of cobalt[14, 15]. Therefore, aluminum is expected to replace a portion of the zinc to reduce the maintenance cost and enhance the corrosion resistance of materials. And then the corrosion behavior of oxide film formed on 316L SS with simultaneous injection of zinc and aluminum was explored and the results showed that this technology effectively improved the corrosion resistance of the oxide film, and new substances $ZnAl_2O_4$ and α-FeOOH with extremely low solubility and high stability were detected in the oxide film[16]. However, in this study, the concentration of zinc and aluminum injected was significantly greater than the actual concentration to enhance effect. In addition, there are few exploratory studies of this technology on other alloys.

The aim of this paper is to investigate effects of simultaneous injection of zinc and aluminum on the corrosion resistance of oxide films formed on 304L SS in simulated PWR primary water by using electrochemical potentiodynamic scan, EIS, Mott-Schottky curve, SEM and XPS analysis. Additionally, the possibility of using aluminum along with zinc, compared to a traditional zinc injection technique, to enhance the corrosion resistance of the oxide film is evaluated.

2. EXPERIMENTAL

2.1. Samples preparation

Austenitic 304L stainless steel was first cut into small pieces of 10 mm×10 mm×4 mm. Then all samples were polished by silicon carbide metallurgical papers from 400 grit to 2000 grit and mirror-polished by 0.3 μm alumina gel. Next, the specimens were rinsed with deionized water, degreased with ethanol and finally washed with deionized water again for 30 min. The samples were dried under a cold airflow and kept in a vacuum glass desiccator. The chemical composition of 304L SS used is shown in Table 1.

Table 1. Chemical compositions of 304L SS

Elements	C	Si	Mn	P	S	Cr	Ni	Fe
Mass, %	0.03	0.52	1.03	0.017	0.006	18.01	9.60	70.77

2.2. Oxidation in simulated PWR primary water conditions

Treated samples were immersed in test solutions in a stainless-steel reaction vessel with a pressure of 6.4 MPa and a temperature of 561±1 K for 144 hours. In LWR primary water, boric acid is added as a neutron absorber and lithium hydroxide as a pH regulator[17]. Thus, a solution containing 250 ppm B^{3+} and 1.1 ppm Li^+ was used as blank solution. The compositions of test solutions are listed in Table 2. B^{3+}, Li^+, Zn^{2+} and Al^{3+} were provided by boric acid, lithium hydrate, zinc acetate and aluminum acetate, respectively. After oxidation, the oxidized samples were taken out of the reaction vessel, cleaned with deionized water and kept in a vacuum glass desiccator.

Table 2. Ionic compositions of the aqueous simulated testing solutions

Test solution	B(III) (ppm)	Li^+ (ppm)	Zn^{2+} (ppb)	Al^{3+} (ppb)
G(blank)	250	1.1	0	0
G(40Zn)	250	1.1	40	0
G(40Zn+20Al)	250	1.1	40	20

2.3. Surface analysis

After oxidation, the oxide films formed on samples obtained under different testing aqueous solutions was characterized using scanning electronic microscopy (SEM), the existence of zinc and aluminum in the oxide film were detected by X-ray photoelectron spectroscopy (XPS), and phase composition of oxide film with extremely thin thickness was detected by grazing incidence X-ray Diffraction (GI-XRD), fixed incident angle was 1° and scanning frequency was 5°/min.

2.4. Electrochemical measurements

All electrochemical measurements (electrochemical potentiodynamic scan, EIS and Mott-Schottky curve) were carried out in triplicate with a PARSTAT2273 potentiostat of Princeton Ltd. in a conventional 150mL three-electrode cell at room temperature. A saturated calomel electrode was used as the reference electrode and a platinum electrode was used as the counter electrode. The exposed area of specimen was 0.2826 cm^2. The electrolyte solution was 0.15 mol/L boric acid + 0.0375 mol/L sodium borate buffered solution (tested pH=8.4) in all experiments. Highly purified N_2 gas was bubbled through electrolyte solution for 40 min before all tests.

The electrochemical potentiodynamic scan test was performed with a scanning range of -0.5 V~1.0 V (with respect to the open circuit potential) at a scan rate of 0.001 V/s, and the corrosion current density was calculated from the test data of weak polarization region. Electrochemical impedance spectroscopy (EIS) was measured at the open circuit potential with a frequency range of 10^6 Hz to 10^{-2} Hz, and equivalent circuit diagram and its fitting parameters were analyzed by using ZSimpwin software. The Mott-Schottky measurement was carried out at a potential range of 1.2 V to -1.0 V, which is within the passivation zone of plarization curve. The amplitude and the frequency of the sinusoidal perturbation signal were 0.01 V and 1 kHz, respectively.

3. RESULTS

3.1. Potentiodynamic scan (polarization curve)

The potentiodynamic polarization curves of oxide films on 304L SS formed in high temperature water were measured in 0.15 mol/L boric acid + 0.0375 mol/L sodium borate buffered solution and are shown in Fig. 1. The corrosion current density (i_{corr}) and corrosion potential (E_{corr}) are shown in Table 3.

It could be seen from the results shown in Fig. 1 and Table 3, compared with that of the blank group, injection of zinc or simultaneous injection of zinc and aluminum effectively reduced the corrosion current and improved the corrosion resistance of the oxide film formed on 304L SS in high temperature water. In compared with specimen G(40Zn), specimen G(40Zn+20Al) showed smaller corrosion current density. It indicated that a simultaneous injection of zinc and aluminum improved more effectively the corrosion resistance of the oxide film than sole injection of zinc.

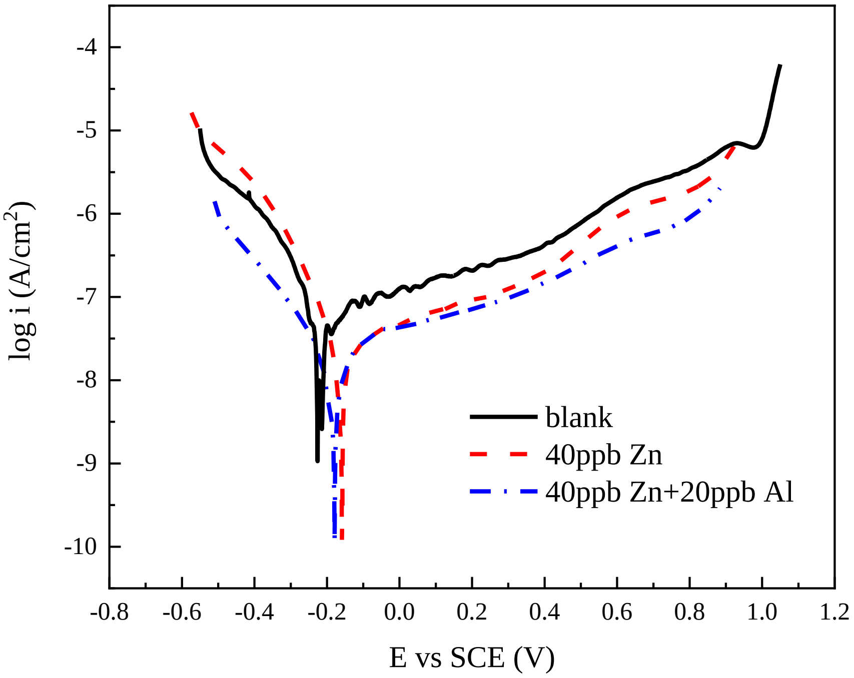

Figure 1. Polarization curves of oxide films formed on 304L SS with different concentrations of zinc and aluminum treatment in high temperature water

Table 3. Corrosion current (i_{corr}) and corrosion potential (E_{corr}) of oxide films formed on 304L SS with different concentrations of zinc and aluminum treatment in high temperature water

Group	i_{corr} (A)	E_{corr} (V)
G(blank)	1.977E-07	-0.228
G(40Zn)	5.286E-08	-0.158
G(40Zn+20Al)	2.147E-08	-0.183

3.2. Electrochemical impedance spectroscopy (EIS)

The oxide films on 304L SS formed under different conditions were characterized by EIS tests in the buffered solution. The Nyquist plots and the Bode plots of the oxide films of 304L SS are shown in Fig. 2a and Fig. 2b, respectively. ZSimpwin software was used to analyse the measured data. The best fitted equivalent circuit and its parameters are shown in Fig. 3 and Table 4, respectively.

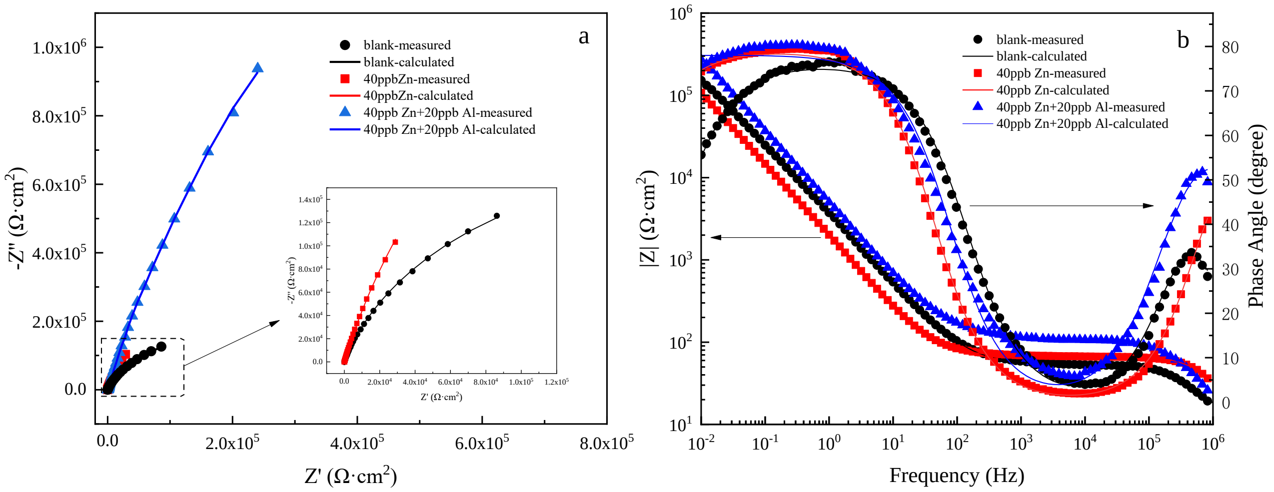

Figure 2. EIS test of oxide films formed on 304L SS with different concentrations of zinc and aluminum treatment in high temperature water: a) Nyquist plots and b) Bode plots

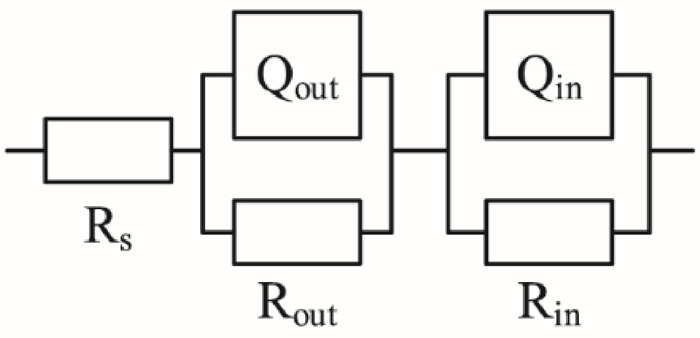

Figure 3. Electrical equivalent circuit diagram of oxide films formed on 304L SS

Table 4. Fitting parameters of EIS test

Group	R_s (Ω/cm^2)	Q_{out}		R_{out} (Ω/cm^2)	Q_{in}		R_{in} (Ω/cm^2)
		Y (S·sec^n/cm^2)	n		Y (S·sec^n/cm^2)	n	
G(blank)	1.429E-01	5.770E-05	0.846	3.966E+01	3.534E-08	0.951	4.125E+04
G(40Zn)	3.039E-01	1.568E-08	0.904	6.811E+01	1.016E-04	0.878	1.429E+06
G(40Zn+20Al)	6.468E-02	6.218E-08	0.859	1.065E+02	4.028E-05	0.868	2.178E+08

As seen from Fig. 2, the EIS data were well fitted to the equivalent circuit model in Fig. 3, which illustrated that the oxide films formed in different solutions had a similar two-layer structure[16, 18], where R_s represents the solution resistance, R_{out} represents the outer layer resistance of the film, and R_{in} represents the inner layer charge transfer resistance of the oxide film. Q is a constant phase element (CPE). And Q has two parameters: parameter Y, which is equal to the equivalent capacitance of oxide film, and parameter n, which is the dispersion index and can be used to evaluate the dispersion effect of the oxide film.

It was evident from the data in Table 4 that injection of zinc or simultaneous injection of zinc and aluminum into high temperature water increased slightly the resistances of outer layer and inner layer of the oxide films. However, simultaneous injection of zinc and aluminum was more effective in increasing the resistance of oxide films than a sole injection of zinc. This may result from increasing in thickness of oxide film or decreasing in conductivity of oxide films with injections of zinc and/or aluminum into high temperature water. In addition, it could be seen that simultaneous injection of zinc and aluminum had the lower dispersion index of the inner layer, which indicated a strong dispersion effect[5, 19].

3.3. Mott-Schottky test

The oxide films of stainless steel are semiconductor, and the semiconductor properties of oxide films exerts a significant effect on the resistance of the oxide films. The Mott-Schottky test is often used to investigate the semiconducting properties of oxide films [20, 21]. The relationship between the space charge capacitance (C) and the potential (E) of an oxide film in a corrosive solution can be described by the Mott-Schottky equation. The relationship between the space charge capacitance (C) and the potential (E) for a n-type semiconductor is as follows:

$$\frac{1}{C^2}=\frac{2}{\varepsilon\varepsilon_0 eN_d}\left(E-E_{fb}-\frac{KT}{e}\right) \tag{1}$$

And for a p-type semiconductor:

$$\frac{1}{C^2}=-\frac{2}{\varepsilon\varepsilon_0 eN_a}\left(E-E_{fb}-\frac{KT}{e}\right) \tag{2}$$

where C represents the space charge capacitance, ε is the vacuum dielectric constant (8.85×10^{-14}F/cm), ε_0 is the dielectric constant of the semiconductor, e is the electron charge (1.602×10^{-19}C), N_d is the donor density, N_a is the acceptor density, E is applied electrode potential, E_{fb} is the flat band potential, T is the test temperature and K is the Boltzmann constant (1.38×10^{-23}J/K). The reciprocal of the square of the charge capacitance (C^{-2}) is linear with the applied electrode potential (E); thus, the semiconductor type can be judged based on a positive (n-type) or a negative (p-type) tangent slope[22]. The carrier concentration (N_d or N_a) and the flat band potential (E_{fb}) in the oxide film can be calculated according to the slope and intercept of the tangent equation, respectively.

The Mott-Schottky plots of the oxide films formed on 304L SS obtained under different zinc and aluminum injection conditions in a range of corresponding passivation potential intervals are shown in Fig. 4.

The oxide films formed on 304L SS in high temperature water showed n-type to p-type semiconducting behavior. With injection of zinc or simultaneous injection of zinc-aluminum, the oxide films showed obvious p-type semiconductor properties. Previous studies stated that the oxide film formed on 304L SS was a double-layer structure[23]. The outer layer generally consisted of iron oxides in different valence states (Fe_2O_3, Fe_3O_4) and iron hydrate ($Fe(OH)_3$), which showed n-type semiconducting characteristics, and the inner layer consisted of chromium oxides in different valence states (Cr_2O_3 and CrO_3), showing p-type semiconducting characteristics[12, 24]. The results shown in Fig. 4 implied that the space charge depletion zone was situated in the inner layer of the oxide film that was consisted of chromium oxides, and the out layer, which was consisted of iron oxides, was in a condition of accumulation.

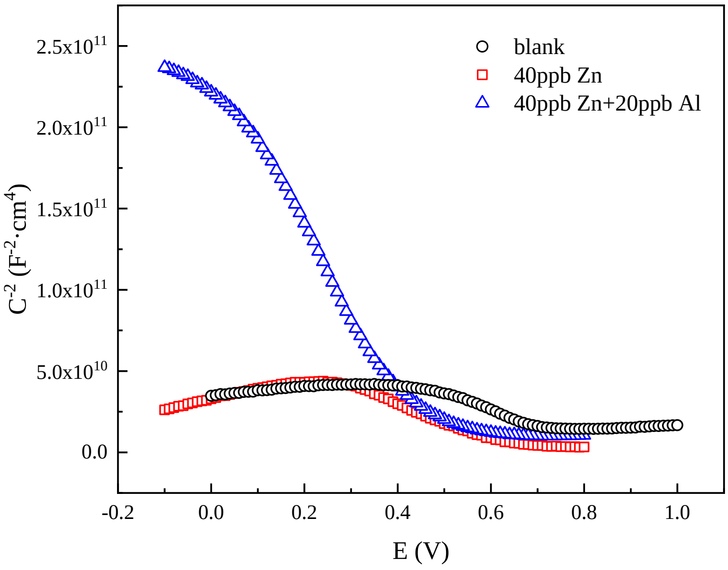

Figure 4. Mott-Schottky curves of oxide films formed on 304L SS with different concentrations of zinc and aluminum treatment in high temperature water

The carrier concentration and the flat band potential data calculated according to the Mott-Schottky equation are listed in Table 5. It could be seen from Table 5, the flat band potential and carrier concentration of the oxide film on 304L SS in high temperature water were decreased by injection of zinc, and were decreased further by simultaneous injection of zinc and aluminum. Because the donor concentration decreased as the carrier concentration decreased[7, 25], the stability and corrosion resistance of the oxide film were enhanced by injection of zinc or simultaneous injection of zinc and aluminum.

Table 5. Carrier concentration (N_d) and flat band potential (E_{fb}) of oxide films formed on 304L SS with different concentrations of zinc and aluminum treatment in high temperature water

Group	N_d (p) (cm^{-3})	E_{fb} (p) (V)
G(blank)	1.22345E+20	0.909
G(40Zn)	1.04285E+20	0.694
G(40Zn+20Al)	2.02909E+19	0.470

3.4. Morphology of the oxide films (SEM)

The SEM images of the oxide films formed on 304L SS in high temperature water with different zinc and aluminum injection conditions are presented in Fig.5a, Fig.5b and Fig.5c, respectively.

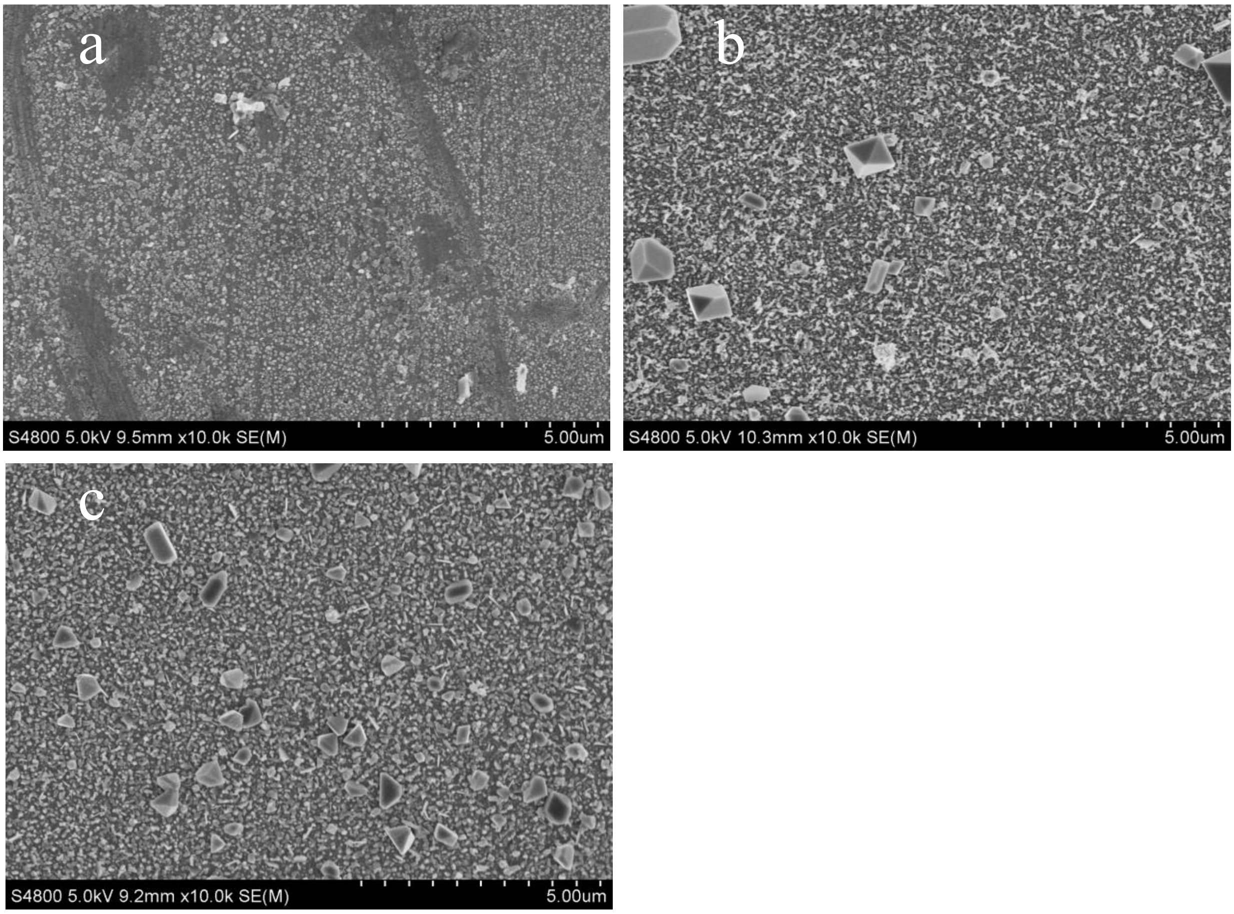

Figure 5. SEM images of oxide films formed on 304L SS with different concentrations of zinc and aluminum treatment in high temperature water: a) G(blank), b) G(40Zn) and c) G(40Zn+20Al) (S4800 5.0kV, ×10.0k)

As seen from the SEM images, oxide film in group G(blank) was loose, and many parts were not protected, and pitting and crevice corrosion were prone to occur. While oxide film in the other two groups was more complete. Compared to injection of zinc, the oxide film formed on 304L SS with simultaneous injection of zinc and aluminum was denser, and the spinel substance with a regular octahedron shape was detected in the oxide film. According to previous research, these kinds of substances might be $ZnFe_2O_4$ and $ZnAl_2O_4$[9, 16, 26], which illustrated that the simultaneous injection of zinc and aluminum could improve the stability and compactness of the oxide film as well as when only injecting with zinc.

3.5. XPS analysis

The XPS spectra of $Zn2p_{3/2}$ of G(40Zn), $Zn2p_{3/2}$ of G(40Zn+20Al) and Al2p of G(40Zn+20Al) are presented in Fig.6a, Fig.6b and Fig.6c, respectively (the binding energy of the C1s photoelectron peak was 284.8 eV).

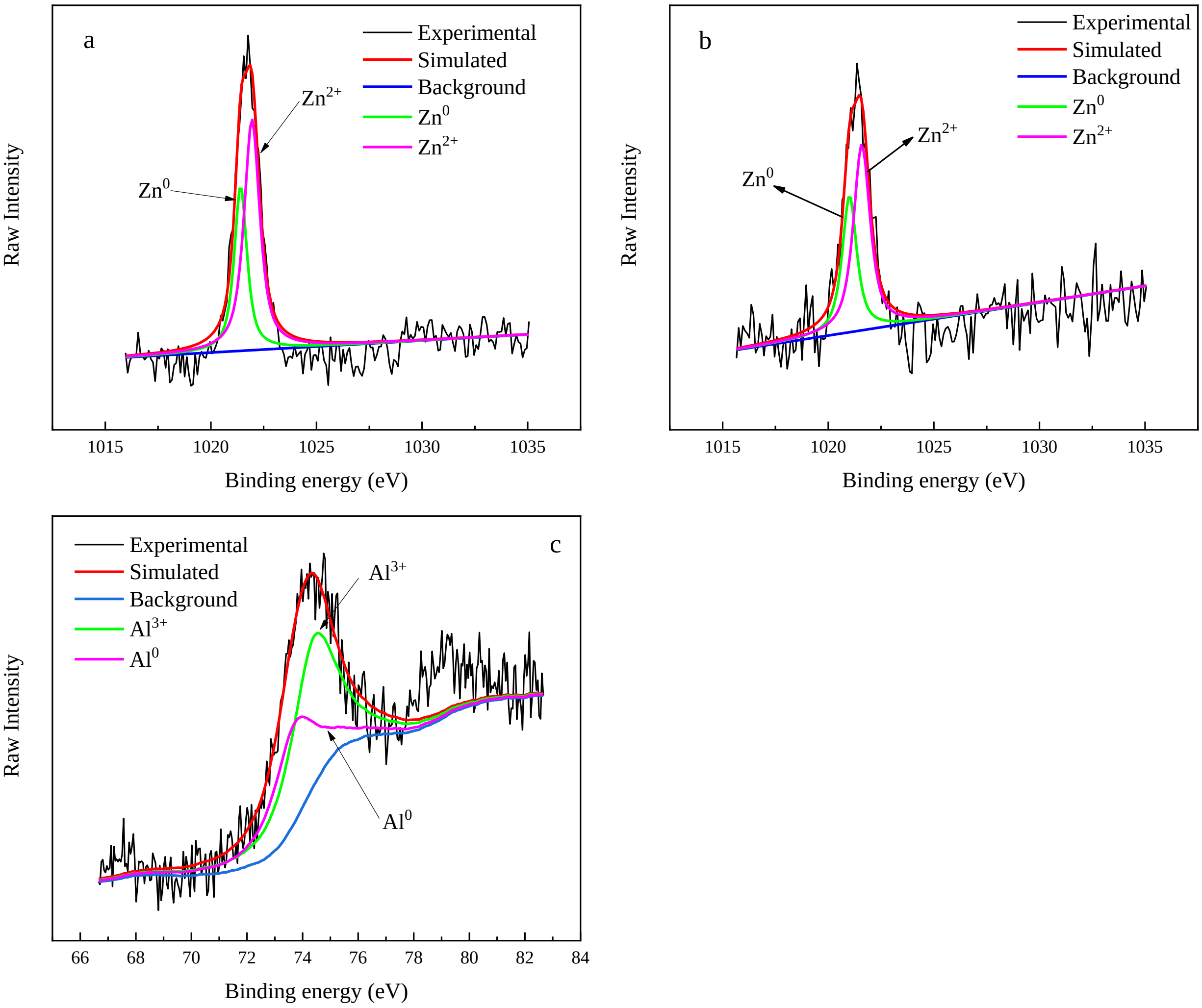

Figure 6. The XPS spectra of oxide films formed on 304L SS with different concentrations of zinc and aluminum treatment in high temperature water (500μm, CAE 30.0): a) $Zn2p_{3/2}$ of G(40Zn), b) $Zn2p_{3/2}$ of G(40Zn+20Al) and c) Al2p of G(40Zn+20Al)

It was obvious from the spectra of $Zn2p_{3/2}$ that the zinc element could be detected in the oxide film of G(40Zn) and G(40Zn+20Al), the peak at the binding energy of 1021.9 eV corresponded to Zn^{2+}[27, 28], which may be ZnO and other zinc-containing spinel oxides. At the same time, the peak of Zn^0 was also present in the spectra (1021.6 eV)[29, 30], but its peak area was much smaller than that of Zn^{2+}.

From the Al2p spectra, aluminum could be detected in the oxide film of G(40Zn+20Al) in the form of Al^{3+} (74.3 eV) and Al^0 (73.8 eV). The content of Al^0 was less than that of Al^{3+}. Al^{3+} may represent the existence of $ZnAl_2O_4$ (74.3 eV), Al_2O_3, γ-Al_2O_3 and $NiAl_2O_4$[31, 32]. The results proved that zinc and aluminum were involved in the film formation reactions of 304L SS in high temperature water, and in combination with the results from previous studies, a $ZnAl_2O_4$ spinel material was formed in the oxide film.

3.6. GI-XRD

The GI-XRD of the oxide films formed on 304L SS with G(40Zn) and G(40Zn+20Al) injection are shown in Fig. 7. It could be clearly seen that zinc ferrite was formed in the oxide film under both conditions, but the amount generated in G(40Zn+20Al) was significantly less than that in G(40Zn). In G(40Zn+20Al), $ZnAl_2O_4$ spinel was also detected, replacing part of original zinc ferrite, which showed that zinc and aluminum simultaneous injection could enhance corrosion resistance by generating new substance in oxide film.

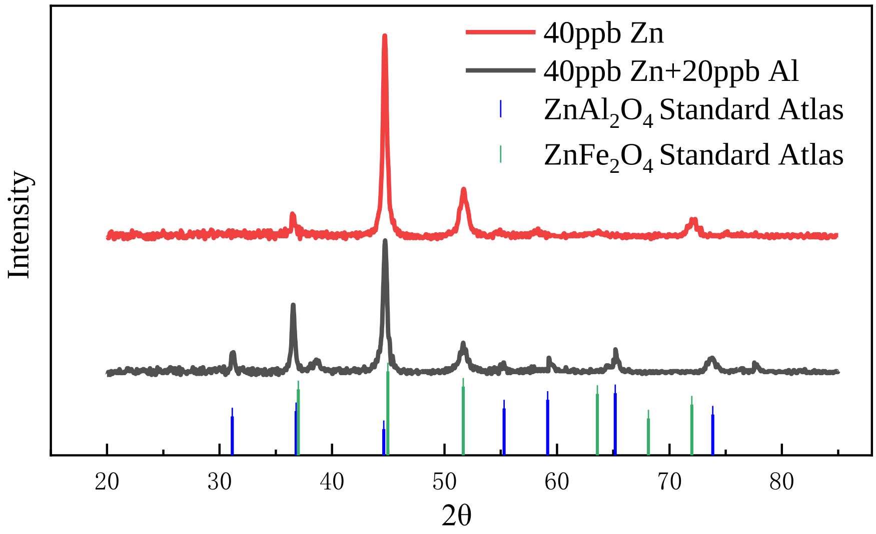

Figure 7. GI-XRD spectra of oxide films formed on 304L SS with G(40Zn) and G(40Zn+20Al) in high temperature water

4. DISCUSSION

Based on the results of the polarization curve and the EIS tests, it could be concluded that the simultaneous injection of zinc and aluminum could reduce the corrosion current density, increase the impedance of the oxide film formed on 304L SS and enhance the corrosion resistance of the oxide film as well as when sole injection of zinc. And compared with the previous studies of aluminum injection alone[14, 15], the improvement of corrosion resistance was more obvious and stable.

Zinc (Zn^{2+}) and aluminum (Al^{3+}) were detected in the oxide film formed by simultaneous injection of zinc and aluminum in the XPS analysis. The zinc and aluminum were involved in the formation of the oxide film, and the binding energy of the Al^{3+} peak corresponded exactly to that of $ZnAl_2O_4$. The SEM image showed that the simultaneous injection of zinc and aluminum caused a large amount of regular octahedral spinel materials to appear in the oxide film and improved the compactness of the oxide film. In addition, results of GI-XRD showed that zinc and aluminum simultaneous injection would produce zinc ferrite and zinc aluminate gahnite in oxide film. These results, combined with the results from previous studies on 316L SS, could infer that the $ZnAl_2O_4$ phase was formed in the oxide film on 304L SS, and the extremely low Gibbs free energy and solubility of $ZnAl_2O_4$ at high temperatures improved the stability of the oxide film[11, 16].

The analysis of the Mott-Schottky curve revealed the change in the semiconducting properties of the oxide film formed on 304L SS. Simultaneous injection of zinc and aluminum made the oxide film exhibit p-type semiconducting properties in which the capacitance was controlled by the inner layer. Meanwhile, the simultaneous injection of zinc and aluminum reduced the flat band potential and carrier concentration of the oxide film. According to the point defect model, the lower carrier concentration reduced the donor concentration, and the stability of the oxide film was enhanced[33, 34]. The formation mechanism of an oxide film on stainless steel has been a subject of intense study for many years. A number of models have been proposed to explain the kinetic, thermodynamic, structural and electronic properties of oxide film formation. Among all the models, the point defect model (PDM) has been widely accepted.

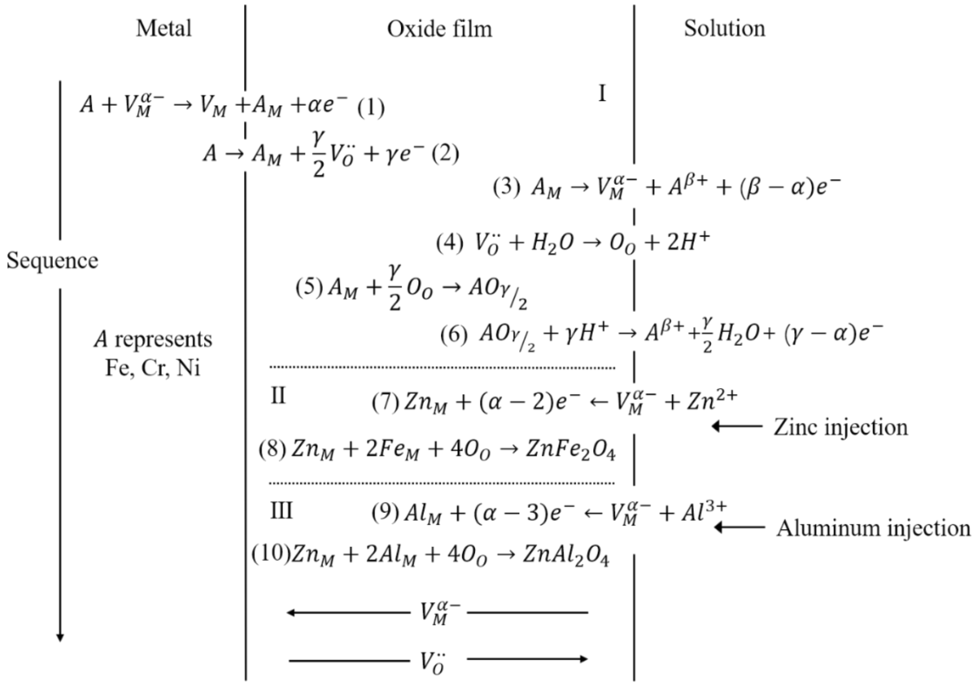

Figure 8. Schematic representation of the growth processes occurred in the oxide film formed on 304L SS based on PDM

PDM microscopically describes the growth process of an oxide film under steady state conditions, and is based on the migration of point defects (oxygen and metal vacancies) under the influence of an electrostatic field in the oxide film. A barrier layer is predicted to grow into the metal by generation and annihilation of the oxygen vacancies at different interfaces[33, 35, 36]. Three assumptions need to be followed in PDM: 1) The oxide film contains high concentrations of point defects; 2) The metal/film and film/solution interface are in electrochemical equilibrium; and 3) The electric field strength in the film is constant. Fig. 8 showed a schematic representation of the growth processes that occurred in the formation of an oxide film on 304L SS according to the basic theory of PDM[37-41].

In Fig. 8, A represents the metal anion (Fe, Cr and Ni), A_M is the metal cation in cation site, V_M is the vacancy in metal phase, O_O is the oxygen ion in anion site, $V_M^{\alpha-}$ is the metal cation vacancy, $V_O^{\cdot\cdot}$ is the oxygen anion vacancy, and $A^{\beta+}$ is the metal ion in solution. In the absence of zinc or aluminum injection (stage I) during film growth and in the steady state, metal cation vacancies were formed at the film/solution interface and consumed at the metal-film interface. Oxygen anion vacancies were produced at the metal/film interface and annihilated at the film/solution interface. Reactions (2) and (5) described the formation progress of metal oxides such as Fe_2O_3, $NiFe_2O_4$, Cr_2O_3, $NiCr_2O_4$ and NiO in oxide film, and reaction (6) accounted for the dissolution of the metal oxides. At this time, the oxygen anion vacancy density was larger than that of the metal cation vacancy, the oxide film conducted electricity from the metal to the solution through free electrons, and the oxide film exhibited the n-type to p-type semiconducting properties of an oxide film formed on 304L SS under normal conditions.

When zinc was injected into the solution (stage II), Zn^{2+} in the solution bound to the metal cation vacancies in the oxide film placing zinc in the cation site (Zn_M), which could be detected as elemental zinc (Zn^0). In addition, reaction (8) led to the formation of $ZnFe_2O_4$, which had been proven to have extremely low solubility and high stability at high temperature, so it became extremely difficult to perform the dissolution reactions. $ZnFe_2O_4$ could be stably present in the oxide film and improved the stability of the oxide film[9]. Meanwhile, the oxygen anion vacancies in the oxide film were gradually consumed, and metal cation vacancies accumulated in the inner layer of the film. The n-type semiconducting property of the oxide film gradually disappeared, and the p-type semiconducting property was increasingly exhibited.

When zinc and aluminum were simultaneously injected into the solution (stage III). In addition to the reactions in stage II, Al^{3+} in the solution was also bound at the metal cation vacancies and entered the oxide film, forming a $ZnAl_2O_4$ phase with zinc cations and oxygen ions as reaction (10). At this moment, elemental aluminum and Al^{3+} could be detected in the film. The stability of $ZnAl_2O_4$ was higher than that of $ZnFe_2O_4$[16], thus further improving the corrosion resistance and stability of the oxide film. In addition, the oxide film was mainly conductive through vacancies, and the p-type semiconducting property was exhibited.

5. CONCLUSIONS

The zinc and aluminum simultaneous injection technique could reduce the corrosion current and increase the impedance of the oxide film formed on 304L SS in high temperature water as well as sole injection with zinc. Simultaneous injection of zinc and aluminum changed the oxide film to p-type semiconducting properties. Both zinc and aluminum were involved in the formation reactions of the oxide film and formed spinel phases of $ZnAl_2O_4$ and $ZnFe_2O_4$ which had regular octahedral structure. The above substances improved the compactness and enhanced the stability and corrosion resistance of the oxide film. In addition, the point defect model was used to microscopically describe the formation process of $ZnAl_2O_4$ and $ZnFe_2O_4$ in the oxide film and the change of semiconducting properties.

ACKNOWLEDGMENTS

This work is supported by the Fundamental Research Funds for the Central Universities (No. 2018QN092); the Natural Science Foundation of Beijing, China (Grant No.2192051).

References

1. M. Hayashi, *Nucl. Eng. Des.*, 184 (1998) 135.
2. H. Tukur and L. Yonghao, *Int. J. Electrochem. Sci*, 15 (2020) 2115.
3. S.A. Maloy, M.R. James, G. Willcutt, W.F. Sommer, M. Sokolov, L.L. Snead, M.L. Hamilton and F. Garner, *J. Nucl. Mater.*, 296 (2001) 119.
4. E. Otero, A. Pardo, M.V. Utrilla, E. Sáenz and F.J. Perez, *Mater. Charact.*, 35 (1995) 145.
5. W. Kuang, X. Wu and E. Han, *Corros. Sci.*, 52 (2010) 4081.
6. R. Nishimura and Y. Maeda, *Corros. Sci.*, 46 (2004) 769.
7. S. Zhang, Y. Tan and K. Liang, *Mater. Lett.*, 68 (2012) 36.
8. F. Arjmand, J. Wang and L. Zhang, *J. Alloys Compd.*, 791 (2019) 1176.
9. S. Zhang, R. Shi and Y. Tan, *J. Alloys Compd.*, 711 (2017) 155.
10. K. Liang, Y. Xu, W. Wang, R. Shi, Y. Tan and S. Zhang, *Int. J. Electrochem. Sci.*, 11 (2016) 10928.
11. X. Liu, X. Wu and E. Han, *Corros. Sci.*, 53 (2011) 3337.
12. S.E. Ziemniak and M. Hanson, *Corros. Sci.*, 48 (2006) 2525.
13. M. Kato, M. Koiwai and J. Kuwano, *Corros. Sci.*, 19 (1979) 937.
14. S. Zhang, X. Song and K. Zhang, *Int. J. Electrochem. Sci.*, 12 (2017) 12037.
15. X. Song, R.A. Khalil, K. Zhang and S. Zhang, Effects of Aluminum Addition on the Corrosion of 316 Stainless Steel in the Simulated Primary Circuit Water of PWR. *International Conference on Energy Development and Environmental Protection (EDEP)*, Guilin, PEOPLES R CHINA, 2017, 141.
16. S. Zhang, R. Shi, Y. Chen and M. Wang, *J. Alloys Compd.*, 731 (2018) 1230.
17. Y. Tan, S. Zhang and K. Liang, *Int. J. Electrochem. Sci*, 9 (2014) 728.
18. J. Lv, W. Guo and T. Liang, *J. Alloys Compd.*, 686 (2016) 176.
19. G. Song, *Cem. Concr. Res.*, 30 (2000) 1723.
20. K. Azumi, T. Ohtsuka and N. Sato, *J. Electrochem. Soc.*, 134 (1987) 1352.
21. R.D. Gryse, W.P. Gomes, F. Cardon and J. Vennik, *J. Electrochem. Soc.*, 122 (1975) 711.
22. T. Karazehir, M. Ates and A.S. Sarac, *Int. J. Electrochem. Sci.*, 10 (2015) 6146.
23. S.E. Ziemniak and M. Hanson, *Corros. Sci.*, 44 (2002) 2209.
24. N.E. Hakiki, M.F. Montemor, M.G.S. Ferreira and M. da Cunha Belo, *Corros. Sci.*, 42 (2000) 687.
25. S. Fujimoto and H. Tsuchiya, *Corros. Sci.*, 49 (2007) 195.
26. M.A. Lahmer, *Surf. Sci.*, 677 (2018) 105.
27. L. Baggetto, N.J. Dudney and G.M. Veith, *Electrochim. Acta*, 90 (2013) 135.
28. J. Ferreira Junior, K. Souza, J. Rossi, I. Costa, G. Trindade and C. Tamachuk, *Int. J. Electrochem. Sci.*, (2016).

29. T. Gross, A. Lippitz, W.E.S. Unger, A. Lehnert and G. Schmid, *Appl. Surf. Sci.*, 78 (1994) 345.
30. R. Inoue, M. Kitagawa, T. Nishigaki, D. Morita, K. Ichino, H. Kusano and H. Kobayashi, *Appl. Surf. Sci.*, 142 (1999) 341.
31. C. Hinnen, D. Imbert, J.M. Siffre and P. Marcus, *Appl. Surf. Sci.*, 78 (1994) 219.
32. P.M.A. Sherwood, *Surf. Sci. Spectra*, 5 (1998) 1.
33. D.D. Macdonald, *Electrochim. Acta*, 56 (2011) 1761.
34. Ž. Petrović, M. Huković, R. Peter, M. Paulose and M. Petravić, *Int. J. Electrochem. Sci.*, 7 (2012) 9232.
35. N. Li, Y. Li, S. Wang and F. Wang, *Electrochim. Acta*, 52 (2006) 760.
36. E. Sikora, J. Sikora and D.D. Macdonald, *Electrochim. Acta*, 41 (1996) 783.
37. Z. Gao, C. Wang, W. Miao, R. Zhu and D. Xia, *Transactions of the Indian Institute of Metals*, 70 (2017) 1337.
38. Y. Li, D.D. Macdonald, J. Yang, J. Qiu and S. Wang, *Corros. Sci.*, (2019) 108280.
39. L. Feng, H. Yang and F. Wang, *Int. J. Electrochem. Sci*, 7 (2012) 4064.
40. D.D. Macdonald, *Russ. J. Electrochem.*, 48 (2012) 235.
41. H. Jain and A. Sharma, *Phys. Chem. Chem. Phys.*, 4 (2002) 3232